Manuscript Submitted to:
Environmental Science & Technology – Air
for Peer-Review on May 1, 2024

Identifying Sources of NO_x emissions from Aircraft through Source Apportionment and Regression Models

Daniel Goldberg[1], Benjamin de Foy[2], M. Omar Nawaz[1], Jeremiah Johnson[3], Greg Yarwood[3], Laura Judd[4]

[1]Department of Environmental and Occupational Health, George Washington University, Washington, DC, 20052, USA

[2]Saint Louis University, St. Louis, Missouri, 63103, USA

[3]Ramboll, Novato, California, 94945, USA

[4]NASA Langley Research Center, Hampton, Virginia, 23681, USA

Abstract

Air quality managers in areas exceeding air pollution standards are motivated to understand where there are further opportunities to reduce NO_x emissions to improve ozone and $PM_{2.5}$ air quality. In this project, we use a combination of aircraft remote sensing (i.e., GCAS), source apportionment models (i.e., CAMx), and regression models to investigate NO_x emissions from individual source-sectors in Houston, TX. In prior work, GCAS column NO_2 was shown to be close to the "truth" in validating column NO_2 in model simulations. Column NO_2 from CAMx was substantially low biased compared to Pandora (–20%) and GCAS measurements (–31%), suggesting an underestimate of local NO_x emissions. We applied a flux divergence method to the GCAS and CAMx data to distinguish the linear shape of major highways and identify NO_2 underestimates at highway locations. Using a multiple linear regression model, we isolated on-road, railyard, and "other" NO_x emissions as the likeliest cause of this low bias, and simultaneously identified a potential overestimate of shipping NO_x emissions. We modified on-road and shipping NO_X emissions in a new CAMx simulation and increased the background NO_2, and better agreement was found with GCAS measurements: bias improved from –31% to –10% and r^2 improved from 0.78 to 0.80. This study outlines how remote sensing data, including fine spatial information from newer instruments such as TEMPO, can be used in concert with chemical transport models to provide actionable information for air quality managers to identify further opportunities to reduce NO_x emissions.

Introduction

Nitrogen oxide ($NO_x = NO + NO_2$) emissions are directly harmful to human health and a critical participant in ozone formation. Many North American cities already have NO_x-limited ozone formation during the warm season[1–3], and the remaining cities should have primarily NO_x-limited conditions in the coming years[4]. Further reducing ozone pollution in metropolitan areas will therefore require improved quantification of NO_x emissions. Exposure to NO_x is also directly associated with asthma exacerbation in vulnerable groups[5,6] and premature death[7,8]. One major limitation of our current observing network is the inability to accurately quantify NO_x emissions on a sector-by-sector basis in a timely fashion, with the exception of continuous emissions monitoring systems (CEMS) on electricity generating units. Additionally, many non-road sources of NO_x emissions, such as industrial or construction emissions, have large uncertainties[9].

Typically, air pollutant emission rates for chemical species such as NO_x are estimated using a "bottom-up" approach, which uses fuel consumption information, spatial surrogates (e.g., road density, population density, locations of known stack emissions), temporal surrogates (e.g., traffic patterns, industrial work schedules) and emission factors (mass of pollutant per mass of fuel burned) to estimate the spatiotemporal patterns of emissions across regions[10,11]. With investments in technology to better understand the spatiotemporal patterns of pollutants (e.g. incorporating real-time traffic data using speed and type of vehicle) and laboratory studies to better estimate the emission factors in a wide range of conditions, these "bottom-up" estimates can be improved[12]. These new and improved estimates can then be incorporated into a chemical transport model and evaluated against observations from ground monitors. Based on this comparison, the emission estimates can be further adjusted and improved if necessary. However, given the complexity of this cycle, "bottom-up" emission estimates typically take many years to compile by a large team of scientists, and subsequently, are delayed in time by several years from the actual emission time.

A complementary method to estimate air pollutant emissions is in using a "top-down" approach. With this method, emissions are back calculated from pollutant measurements acquired across an entire airshed. This is typically done with a remote sensing instrument – in orbit[13–15] or on an aircraft[16–18]. Analyses have been conducted for global megacities[19–23] and power plants[24,25] using the Tropospheric Monitoring Instrument (TROPOMI) and a complementary satellite instrument, the Ozone Monitoring Instrument (OMI). The emission rates are inferred by analyzing the concentration maps over a large region and incorporating the lifetime (chemical and dispersion lifetime) of the pollutant to back-calculate the emission rate at the source. The advantage of a "top-down" technique is that it is independent of the complex datasets needed to estimate "bottom-up" emissions rates. Typically these aggregated "top-down" estimates agree with the "bottom-up" estimates within 40% in North American cities (well within the uncertainty associated with the 'top-down' method)[13,26]. Given TROPOMI's spatial resolution (3.5×5.5 km^2 at nadir) and temporal resolution (once daily), TROPOMI is most often used to calculate total emissions aggregated over the entire metropolitan area and seasonal/annual timescales, and assumptions are needed to infer emissions rate during morning and evening hours. Therefore, very limited, if any, sectoral or hourly information can be gleaned from an analysis using polar-orbiting satellite datasets, such as TROPOMI.

In this project we used fine spatial resolution nitrogen dioxide (NO_2) information (250×560 m^2) from the Geostationary Coastal and air pollution events Airborne Simulator (GCAS) instrument[27,28], available during the September 2021 NASA/TCEQ Tracking Aerosol Convection ExpeRiment – Air Quality (TRACER-AQ) field campaign[29], to better understand the fine-scale structure of NO_x emissions in the Houston metropolitan area including a sector-by-sector analysis. Complementing the airborne observations, we perform a simulation using the Comprehensive Air Quality Model with Extensions (CAMx) at fine spatial resolution (444×444 m^2). The model output has already been compared to data from GCAS and TROPOMI in a complementary paper[30]. In this project, we push further by using source-tagged NO_2 information from CAMx and GCAS data to estimate more accurate contributions from different NO_x emission sectors. We do this by using flux divergence methods on the GCAS data and by training a multiple linear regression model to the airborne retrievals, with the CAMx source-tagged NO_2 as the independent variables.

Methods

GCAS. The GCAS instrument was installed on the NASA G-V aircraft during the Tracking Aerosol Convection. ExpeRiment – Air Quality (TRACER-AQ) field campaign in Houston, Texas during September 2021. The GCAS instrument employs charge-coupled device array detectors to observe backscattered light. These data can be used to calculate column densities of gases, such as NO_2, below the aircraft using differential optical absorption spectroscopy (DOAS)[31].

During TRACER-AQ, GCAS collected data over the Houston metropolitan area across 12 days during late August and throughout September 2021. The flight strategy of the aircraft included flying the plane in a 'lawnmower' fashion with flight lines spaced 6.3 km apart, ensuring overlap at flight altitude (28,000 feet) with the instrument field of view of 45 degrees creating one gapless map of NO_2 up to three times per flight day. GCAS has a native pixel resolution of approximately 250 m × 250 m at flight altitude. Observations from two of the flight days – a test flight (August 30) and a flight over the Gulf of Mexico (September 27) are excluded from this study because they provided no meaningful data over Houston. Given the relatively short timeframe of flight data collection; meteorological conditions have an influence on the fine-scale patterns in NO_2 columns observations.

Air mass factors use modeled scattering weights and vertical profile information to account for altitude-dependent sensitivities in remote-sensing observations[32,33]. The original vertical profiles in the dataset were derived from a global model, GEOS-CF[34], that had a coarser spatial resolution (0.25° × 0.25°), but in this study we only show GCAS column NO_2 measurements processed with vertical profile information from CAMx. To directly compare GCAS measurements to the CAMx NO_2 column concentrations we re-grid them to the fine-scale WRF-CAMx grid. Only cloud-free GCAS data is considered in this analysis. An example of daily and monthly averaged GCAS data is shown in Figure 1. The differences in these two timescales highlights the complexity of NO_2 variance in cities, such as Houston. Diurnal column NO_2 patterns are shown in Figure S1.

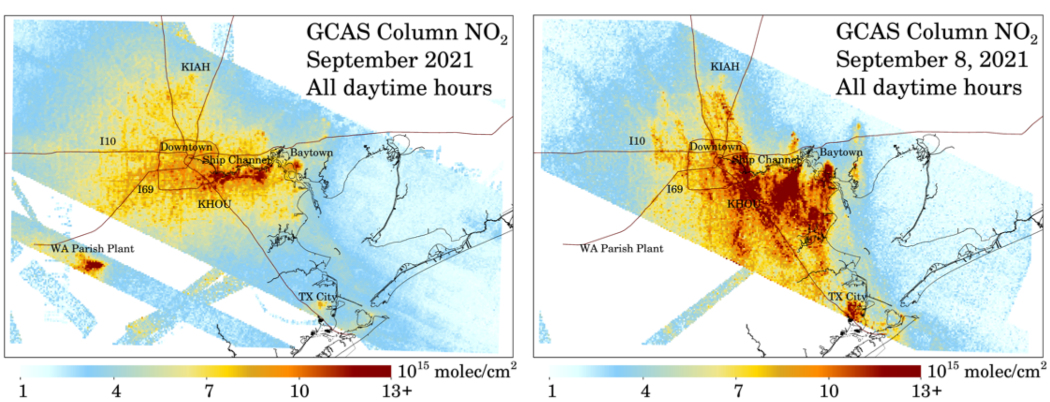

Figure 1. GCAS Column NO_2 measurements during the September 2021 Houston TRACER-AQ field campaign. Left panel showing all GCAS measurements during ten flight days between September 1 – 26,

2021 averaged together. Right panel showing all measurements during the September 8, 2021 flight day averaged together. Areas of large NO_x emissions are labeled on both panels.

Pandora. Observations from three Pandora monitoring sites were available during the TRACER-AQ field campaign to validate the GCAS, satellite, and model column NO_2 measurements. Critical to this project, we found in previous work[30] that the GCAS measurements of column NO_2 during the TRACER-AQ campaign had an excellent correlation ($r^2 = 0.79$) and minimal normalized mean bias (NMB = +3.4%) when compared to measurements of the same quantity from Pandora instruments, suggesting that the GCAS measurements acquired during the TRACER-AQ campaign are very close to the "truth". The Pandora instruments were located in the suburban and urban neighborhoods.

WRF-CAMx simulation. For this study, a set of simulations were conducted employing version 4.3.3 of the Advanced Research Weather Research and Forecasting (WRF) model[35] jointly with the Comprehensive Air Quality Model with Extensions (CAMx) v7.20[36] with the CB6r5 chemical mechanism for a simulation period that matched the September 2021 TRACER-AQ domain and timeframe. The 36/12/4/1.33/0.444 km model domains can be seen in Figure S2. Prior work evaluated this WRF simulation and found minimal systematic biases in surface-level wind speed, direction, temperature, and water vapor mixing ratio compared to observations from sixteen ground-level monitors[30]. A longer description of the WRF-CAMx model options is included in the supplemental including the WRF physics options (Table S1), vertical layer mapping from WRF to CAMx (Table S2), and CAMx science options (Table S3). For emissions in CAMx, we start with an emissions inventory developed by the TCEQ for the Dallas-Fort Worth (DFW) and Houston-Galveston-Brazoria (HGB) Attainment Demonstration (AD) SIP revisions and implement further minor changes as discussed in the Supplemental.

Source Apportionment. We used the CAMx OSAT source apportionment tool to track NO_2 from several emission source sectors as listed in Table S4. To select individual electric generating units (EGUs) in our 0.444 km CAMx domain for NO_2 tracking we used a threshold of 0.8 tons per day of NO_x emissions. This threshold identified nine EGUs shown in the first nine rows of Table S4. We also selected on-road mobile, railyards, shipping and the George Bush Intercontinental (KIAH) and William P. Hobby (KHOU) airports for NO_2 tracking. All remaining NO_x emissions were tracked together in the "other" category. Relevant for this project, average weekday NO_x emissions for the 0.444 m domain were 372.9 tons per day (123 Gg/yr). The total amount of NO_x emissions in each sector can be seen in Table S5 and Figures S3 and S4. Examples of the NO_2 source apportionment can be seen in Figure 2.

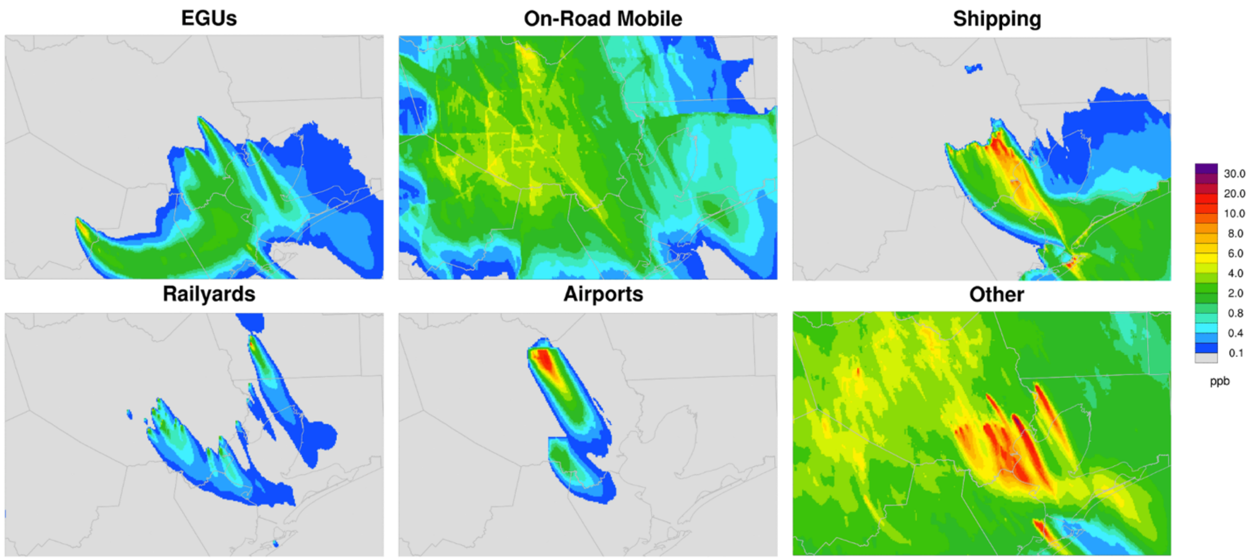

Figure 2. Examples of six of the CAMx tagged surface NO_2 concentrations at 8:00 AM local time on September 8, 2021.

Flux divergence top-down emissions quantification. The flux divergence method can identify point sources in the TROPOMI NO_2 retrievals with higher resolution than averaged vertical column densities. The method was first applied over Riyadh, Germany and South Africa to estimate NO_x emissions from large point sources[15,25]. Due to TROPOMI's higher spatial resolution compared with OMI, the flux divergence method can identify emissions within individual urban areas[26,37–39].

The flux divergence method works best with long temporal averages; for TROPOMI analyses, annual or multi-year averages are used. We adapted the method for the current project to handle GCAS data from 27 individual scenes spanning 10 days. We found that the method worked best when the GCAS data was oversampled to the 444 × 444 m^2 CAMx grid. Only pixels with an aircraft roll angle below 0.5° were used. We interpolated the WRF-CAMx winds to the time of the GCAS overpass. We used second-order differences and performed the flux divergences along the x/y axes (i.e., using the cells to the north, south, east, and west of the central cell). We also calculated the flux divergence for the cross-terms (i.e., using the cells to the north-east, south-east, south-west and north-west of the central cell). Averaging both the x/y estimate and the cross-estimate led to smoother divergence fields with less noise.

The method was initially performed using the GCAS standard retrievals and the ERA5 wind reanalysis product[40]. While this gave good results, we found that the level of noise was reduced and the known sources were better identified when we used the GCAS retrievals that were corrected using the CAMx air mass factors, and when we used the WRF-CAMx meteorology. These sensitivity tests revealed that CAMx simulations can be used to yield clear improvements in the flux divergence method.

Multiple linear regression model. For this study, we built a multiple linear regression (MLR) model to find the optimal combination of the sectoral emissions simulated by CAMx that matches the GCAS tropospheric vertical columns. CAMx simulations were made in Source Apportionment mode to separate the NO_2 vertical column densities associated with the 15 individual sources (e.g., EGU) and groups of sources (on-road mobile) (Table S4). In practice, some of the emission sources in OSAT are too close together to be able to be clearly distinguished from each other. We therefore merged the following: 1. Channelview Cogeneration Facility and Odyssey Energy Altura Cogen, LLC; 2. Deer Park Energy Center and Pasadena Power Plant; 3. Texas City Cogeneration, South Houston Green Power Site, and the "other" category. Equation 1 shows the MLR model: the tropospheric vertical column density of GCAS is represented as an optimal combination of the CAMx VCD from the 10 contributing sectors with a residual given by ε. . In seeking an optimal match to the GCAS columns, it is important to apply a regularization term to prevent unphysical results[41]. The optimal parameters (β) were determined by minimising the cost function in Equation 2. The residual ε is minimised subject to the regularization parameter λ applied to the magnitude of the scale factors (β). Equation 2 can be solved in a single Least Squares inversion[41]. We applied the MLR model to the entire field campaign, and we also performed simulations separately for weekdays and for weekends.

$$VCD_{GCAS} = \sum_{i=1}^{10} \beta_i VCD_{CAMx,i} + \varepsilon \quad (1)$$

$$J = \|\varepsilon\|_2 + \lambda^2 \|\beta\|_2 \quad (2)$$

The regularization term, λ in Equation 2, imposes a cost on the departure of the posterior emissions from the prior emissions. In this work, we chose a value of 25 because it balances the desire to maximize the improvements in the model (lower grid residuals) while minimizing the departure from the prior (lower emission residuals). By selecting this value, we achieve most of the improvements in the correlation coefficient of the model without ending up with unrealistic scaling factors. The algorithm then balances the cost in the change of the emissions with the cost of the mismatch between the GCAS retrievals and the sum of the scaled fields from the source apportionment simulations. We assume as a prior that all scaling factors are 1.

Results and Discussion

The first step in this project is to qualitatively compare the GCAS column NO_2 measurements with coincident measurements from TROPOMI and model output from CAMx. Spatial plots of column NO_2 in the early afternoon at the TROPOMI overpass time are shown in Figure 3 for a 10-day average and a single day. By observing the 10-day average (top row), we can see that GCAS measurements are generally larger than both the TROPOMI measurements and CAMx model output. TROPOMI captures the broad spatial patterns observed by GCAS with a notable low bias. The TROPOMI low bias is partially driven by the 3.5 x 5.5 km^2 spatial resolution which is unable to capture the peaks of the NO_2 pollution, especially the NO_2 in narrow point source plume[42]. Previous work shows that the air mass factor is a small contributor to this low satellite bias in this area[30], but this can vary by region[43]. The low satellite bias is consistent with comparisons completed by the TROPOMI Cal-Val team[44].

The GCAS versus CAMx intercomparison suggests that the point source plumes are captured by the model with decent accuracy, but that NO_2 is severely underestimated in the downtown area of Houston, as well as in the outer portions of the model domain. This suggests two issues with the NO_2 in CAMx: an underestimate of NO_x emissions near downtown Houston, and an underestimate of NO_2 advected into the model domain from the boundary conditions. In following sections, we explore these model biases quantitatively.

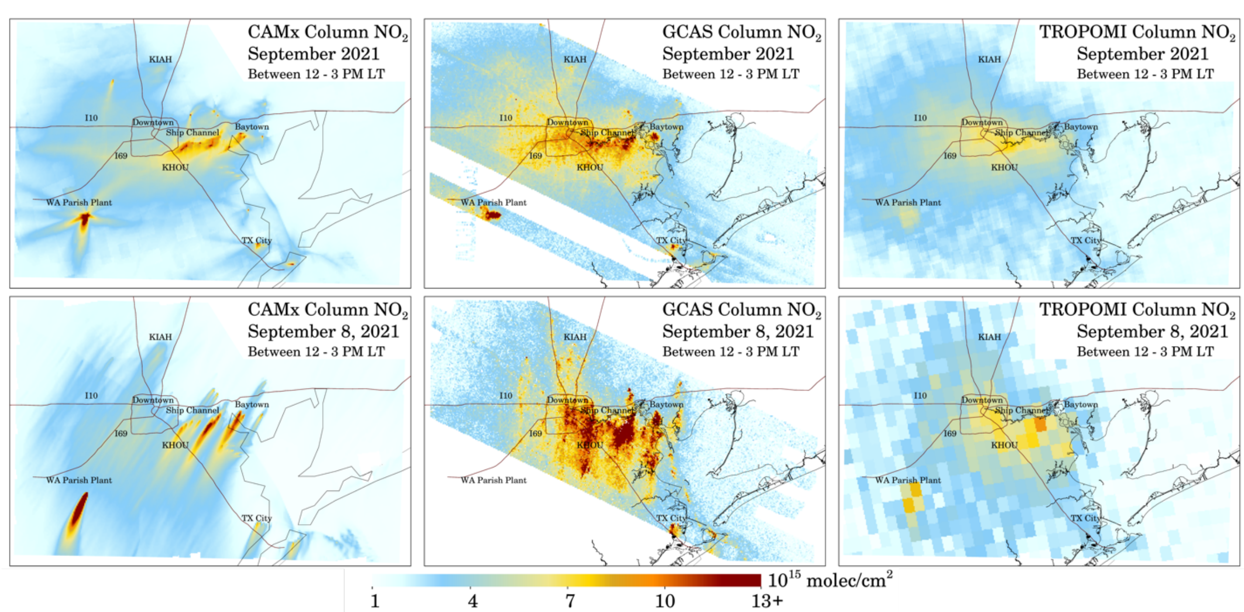

Figure 3. Column NO_2 over Houston from two remote sensing observational platforms, and CAMx model simulation in the early afternoon: 12 – 3 PM local time. Left column shows measurements from TROPOMI, center column shows measurements from GCAS, and right column shows the CAMx model. Top row shows measurements during all 10 flight days in September 2021, while bottom row shows September 8, 2021 only.

NO_x emissions using Flux divergence applied to GCAS. The flux divergence (FD) method applied to the GCAS aircraft data quantified NO_2 fluxes (μg/m^2). To our knowledge, this paper is the first to quantify NO_2 fluxes by applying the FD method to aircraft remote sensing data. We identified many of the major NO_x sources individually in the Houston CAMx domain: power plants and refineries as well as the IAH international airport (Figure 4 left panel). In addition, the method identified the area of the ship channel as well as the route of the ships sailing through the Galveston Bay. Finally, the method clearly identified the major highways in the region. The center panel of Figure 4 shows the flux divergence method applied to the CAMx simulation. In this case, the sources are known and so these simulations serve to evaluate the accuracy of the method. The method clearly recovers the main point and line sources used in the CAMx simulations. The right panel of Figure 4 shows the ratio of the NO_2 flux divergence (i.e., (CAMx-GCAS)/GCAS) for the GCAS grid cells exceeding 0.2 μg-m^2-s^{-1}. Over the large point sources near the ship channel, the values are a mix of positive and negative values suggesting that the emissions inventory is relatively accurate in this location. Over highways, the values are strongly negative suggesting that actual on-road emissions may be underestimated in the current inventory used as input to the CAMx model. In theory, the 444 m spatial resolution model should be capturing the near-road NO_2 concentrations with the same precision as the GCAS which has similar spatial resolution. Over the ship paths, especially closer to the Gulf of Mexico, the values are positive suggesting that some of the ship NO_x emissions may be overestimated in the inventory.

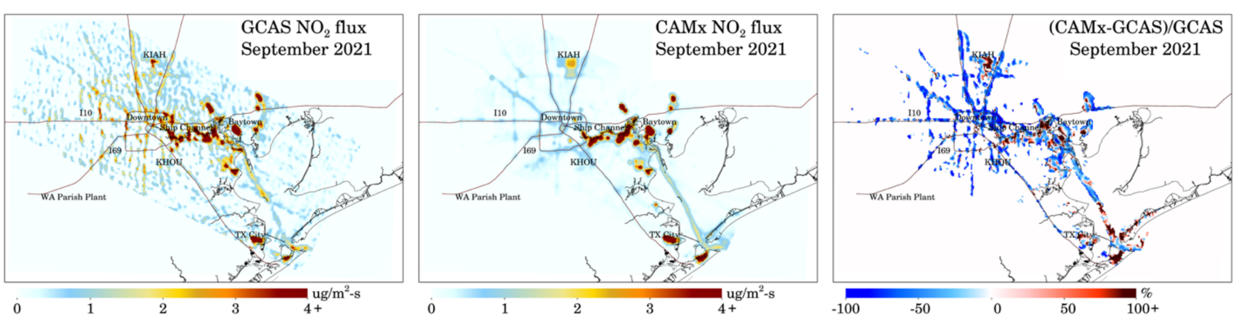

Figure 4. Left panel shows the net NO_2 fluxes (μg/m^2-s) using the FD method applied to all GCAS measurements. Fluxes are positive when there are NO_x emissions originating from a grid cell, fluxes are negative if there is a net NO_x sink in a grid cell. Center panel shows the net NO_2 fluxes (ug/m^2) using the FD method applied to all coincident CAMx output. Right panel is the ratio (CAMx-GCAS)/GCAS in areas where the GCAS NO_2 fluxes are >0.2 ug/m^2-s.

Use of machine learning to estimate emission factors for individual sectors. We applied the MLR model to CAMx source apportionment NO_2 sectoral output and GCAS NO_2 data, as shown in Equations 1 and 2, to estimate scaling factors for the sectoral NO_2. All median scaling factors were between a value of 0.5 and 2.5 as shown in Figure 5. A median value below 1 indicates the sector needs a NO_x decrease, while a median value greater than 1 indicates the sector needs a NO_x increase. The box-and-whisker plots represent the uncertainties of the scaling factors quantified by bootstrapping on two different levels. The most important level for bootstrapping was randomly selecting, with replacement, the GCAS rasters included in the optimization. For the full time series, there were 27 rasters over 10 days. In addition to performing the simulations for these 27 rasters, we performed 100 simulations with random selections of the 27 rasters. The second level for bootstrapping was to randomly select grid blocks within each raster for use in the analysis. We randomly select 7 x 7 blocks of cells within the CAMx grid cells and include them until we have the same number of points as in the initial grid. We did this 100 times for each selection of rasters, leading to a total of 10,000 simulations.

The box-and-whisker plots in Figure 5 show that on-road mobile NO_x emissions representing 19% of domain emissions may be underestimated in the model and need to be scaled up by a median factor of 1.68, which is consistent with findings using the FD method. Similarly, the MLR found railyard NO_x emissions should by increased by a median factor of 1.5. In contrast, the shipping NO_x emissions representing 17% of domain emissions may be overestimated and should be scaled by a median factor of 0.77, which is also consistent with findings using the FD method, though it should be noted that the sign of the shipping adjustment changes with the regularization factor. The EGU point sources are close to a scale factor of one, which is expected given the use of emissions obtained from CAMPD measurements. The "other" sources representing 54% of domain NO_x emissions are underestimated, although this factor is particularly sensitive to the regularization factor because it encompasses a diverse set of point and nonpoint sources. Finally, the boxplot suggests that the NO_2 background concentration is underestimated by CAMx by a median value of 0.7×10^{15} molec/cm^2, which equates to a scaling factor of 2.2, and is consistent with qualitative findings discussed earlier.

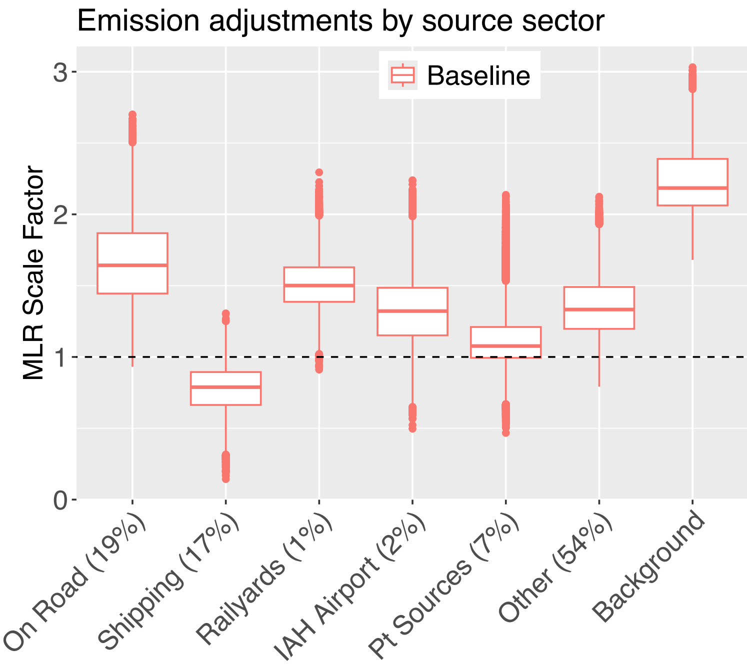

Figure 5. Box-and-whisker plot of scaling factors obtained from the Multi Linear Regression Model with 100 bootstrapped selection of rasters each consisting of 100 bootstrapped selection of grid blocks included in the analysis. Percentages show the fraction of domain-wide NOx emissions from each sector.

Results from an "Optimized NOx" CAMx simulation. We then performed a new "Optimized NOx" CAMx simulation with on-road mobile and shipping NO_x emissions adjusted to be in alignment with findings from using the MLR. On-road mobile NO_x emissions were increased by a factor of 1.68, and shipping NO_x emissions were decreased by multiplying by a factor of 0.77. Despite a large change to the on-road NO_x, the total NO_x emissions in the domain only increased by 8.6% from 373 to 405 tons per day (Table S5). We chose not to adjust the railyards and airport sectors because combined they represent less than 3% of domain NOx emissions. We chose not to adjust the "other" sector or background / boundary NO_2 since there is no straightforward modification for those contributions.

When comparing the column NO_2 from the Baseline and "Optimized NOx" simulations to the GCAS measurements, we found better agreement and an improvement in bias, albeit a smaller improvement than we had expected (Figure 6). The column NO_2 low bias improved from –30.6% to –25.2% with a small increase in correlation from r^2=0.78 to r^2=0.80. When we further add an artificial 0.7 x 10^{15} molec/cm^2 column NO_2 enhancement domain-wide – value acquired from the MLR – the NO_2 low bias improves further to –10.0%. The remaining low bias is likely due to not adjusting the "other" NO_x emissions, which represented 54% of domain NO_x emissions in the Baseline simulation.

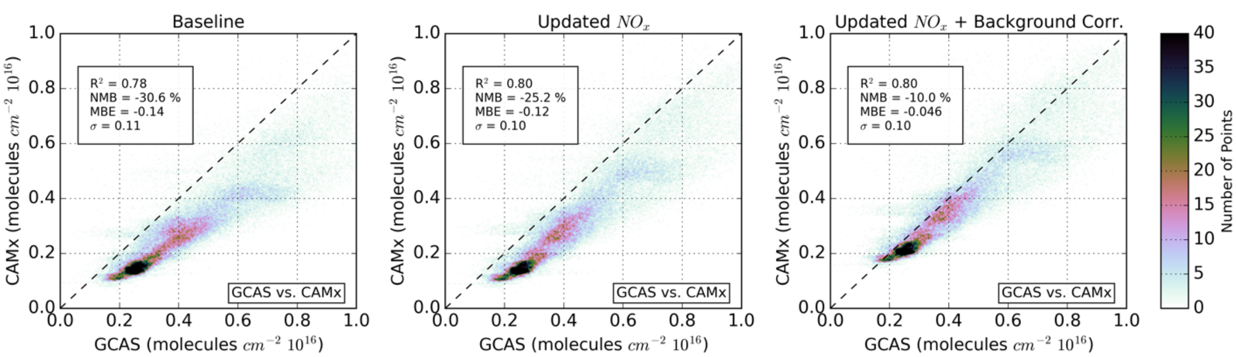

Figure 6. CAMx column NO_2 evaluated against the same quantity from GCAS measurements. Left panel is the baseline simulation. Center panel is the "Optimized NO_x" simulation (1.68x on-road mobile and 0.77x shipping). Right panel is "Optimized NO_x" simulation + an additional 0.7 x 10^{15} column NO_2 background NO_2 using scaling factor from the MLR.

When comparing the column NO_2 from the Baseline and "Optimized NOx" simulations to the Pandora measurements, we found better agreement and an improvement in bias, albeit a smaller improvement than we had expected (Figure 7). The column NO_2 low bias improved from -20.2% to -17.8% with a small increase in correlation from r^2=0.39 to r^2=0.41. However, much of the apparent low bias appears to be driven by the large Pandora measured values. When then exclude values exceeding 10e15 molec/cm^2 – which approximate fine-scale NO_2 plumes that we cannot expect CAMx to recreate in space due to the need to match wind speed and direction. For moderately polluted scenes (values <10e15), the NO_2 low bias is only -6.8%. When evaluating the new model simulation improved from -6.8% to -3.4%; the correlation is notably poor in both scenarios due to the smaller range of values.

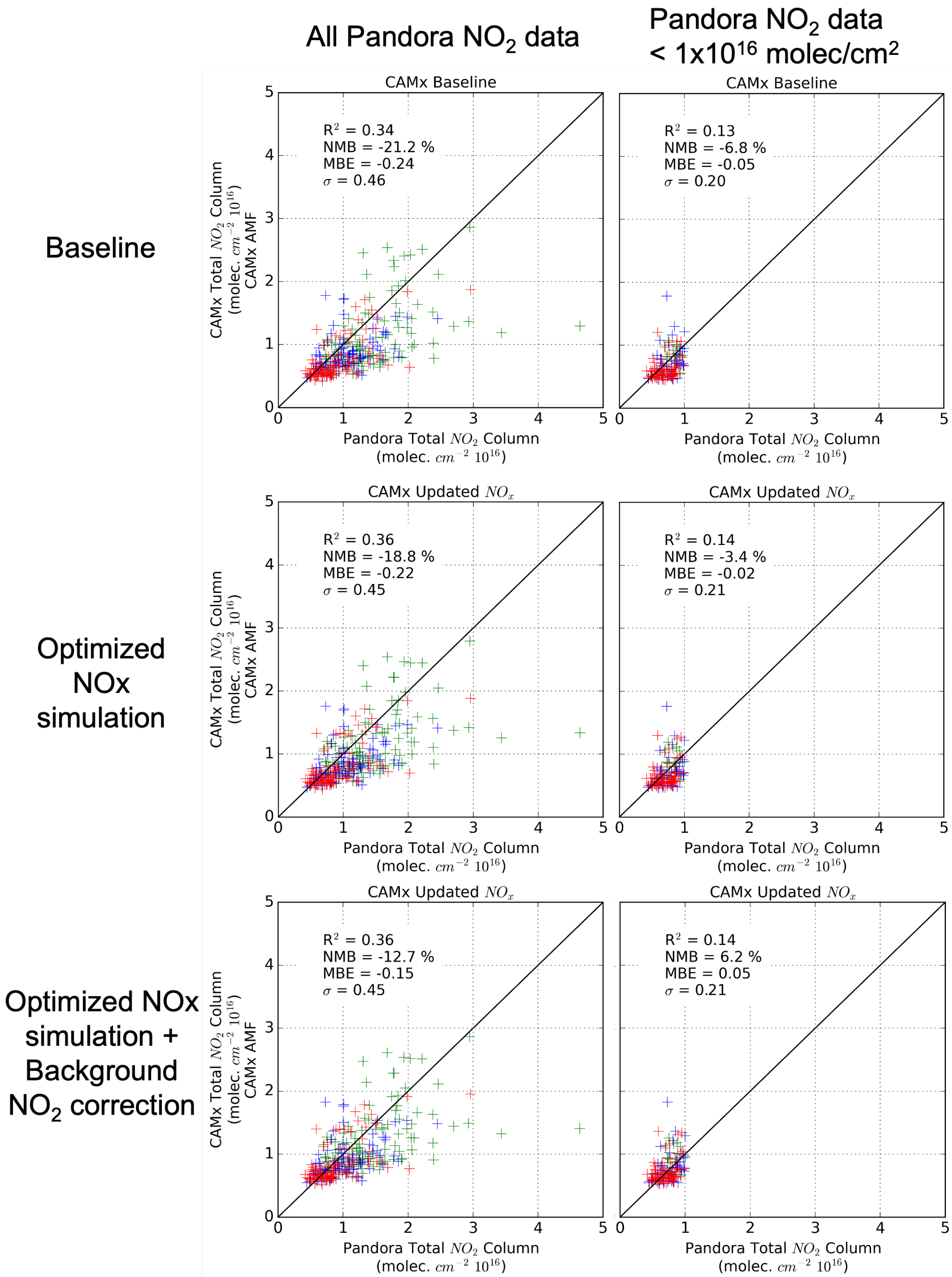

Figure 7. CAMx vs. Pandora total column NO_2 intercomparisons. Left column shows intercomparisons during all conditions. Right column shows intercomparisons during moderately polluted and clean conditions (< 10 x 10^{15} molec/cm^2). Top row shows the baseline CAMx simulation. Middle row shows the "Optimized NOx" CAMx simulation. Bottom row shows the "Optimized NOx" CAMx simulation + Background NO_2 correction (a uniform addition of 0.7 x 10^{15} molec/cm^2). Different colors represent the three Pandora measurement sites as discussed in Nawaz et al., 2024.

Figure 8 shows a ratio difference plot of modeled column NO_2 between the Baseline and "Optimized NOx" simulations. The largest NO_2 enhancements in the "Optimized NO_x" simulation occurred in areas of west Houston where there were no Pandora measurements (denoted as square boxes on the figure). The maximum change in column NO_2 was an increase of 29.6% in west Houston near a major highway intersection, with a median column NO_2 enhancement of +4.2% across the full model domain. Although the model domain NO_x emissions increased +8.6%, column NO_2 only increased +4.2% because a substantial amount of NO_2 originates beyond the model domain.

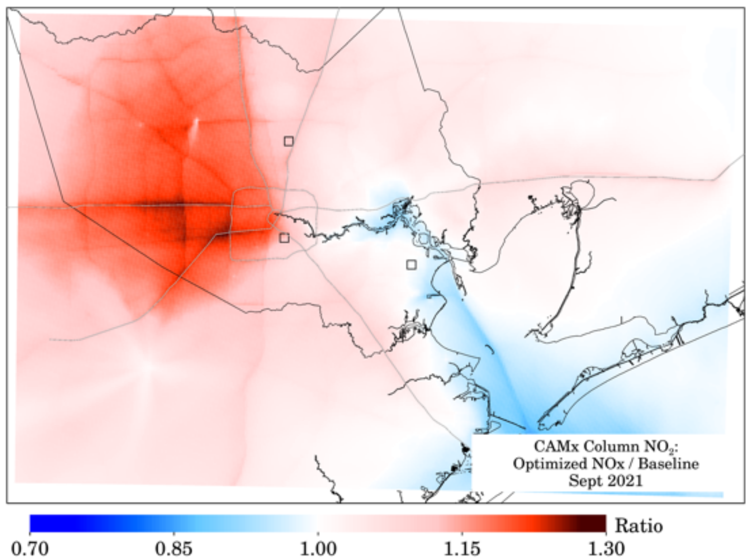

Figure 8. Column NO_2 ratio plot between the CAMx "Optimized NOx" simulation vs. CAMx baseline simulation during the early afternoon (12:00 – 15:00 local time).

When comparing the MLR results between the Baseline and Optimized NOx simulations, we see substantial improvement in the coefficients attributed to on-road and shipping emissions (Figure 9), while all other coefficients remain largely steady. This indicates both the robustness of the method as well as a strong indication that the adjustments made to the NO_x emissions were appropriate. The on-road NO_x emissions may have been slightly overcorrected, and the "other" NO_x emissions still need an adjustment up. As expected, the coefficient attributed to the background NO_2 did not change, and this would be more difficult to control without modifying the boundary conditions or the NO_2 lifetime. A longer discussion on the influence of NO_2 long-range transport on the MLR can be found in the supporting information.

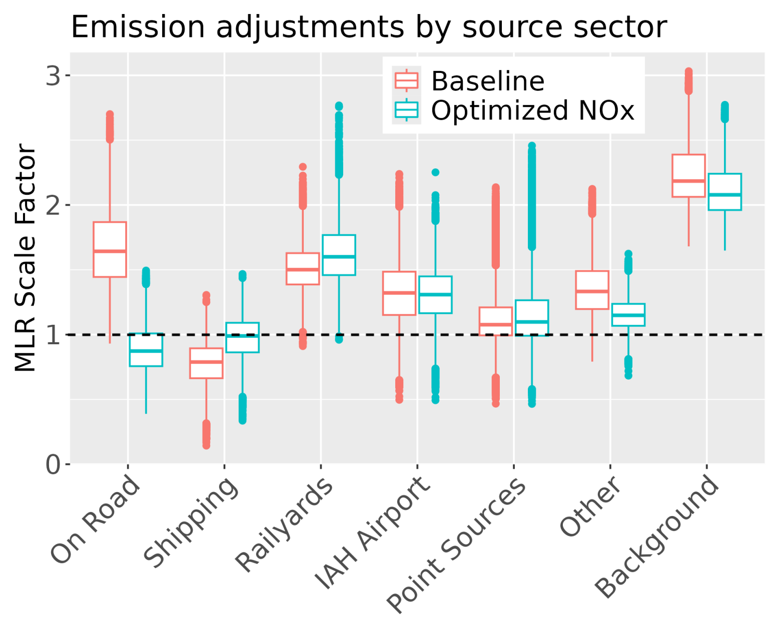

Figure 9. Box-and-whisker plot of scaling factors of the baseline and updated CAMx simulation obtained from the Multi Linear Regression Model with 100 bootstrapped selection of rasters and 100 bootstrapped selection of grid blocks to include in the analysis.

Discussion. In this project, we were able to conduct a thorough analysis of NO_x emissions in Houston, Texas during September 2021 during the TRACER-AQ campaign. Prior work found column NO_2 from GCAS to have excellent agreement with Pandora measurements (r^2=0.79 and NMB of +2.4%)[30], suggesting it can be used as the "truth" in validating the column NO_2 CAMx model simulation. Column NO_2 from CAMx showed a substantial low bias when compared with Pandora (–20%) and GCAS measurements (–31%), suggesting an underestimate of local NO_x emissions.

This study expands upon previous work[30] by applying additional measures to identify and quantify the magnitude of NO_x emissions. The FD method was able to distinguish the linear shape of major highways, many of the large point sources, and the Galveston Bay ship track. The NO_2 FD comparison between CAMx and GCAS shows underestimates at highway locations. Through a multiple linear regression model, we were able to isolate on-road, railyard, and "other" NO_x emissions as the likeliest cause of this low bias, while simultaneously finding that shipping NO_x emissions may be overestimated. A new "Optimized NO_x" simulation was performed with on-road NO_x emissions increased by a factor of 1.68 and shipping NO_x emissions decreased by a factor of 0.77, and confirmed that these NO_x adjustments made to the inventory were reasonable and yielded better agreement with NO_2 measurements acquired during the TRACER-AQ campaign.

To our knowledge, this is the first time a source apportionment model was coupled with aircraft measurements to identify uncertainties in the gridded NO_x emissions inventory. Our analyses were primarily conducted using column NO_2 instead of surface NO_2 to diagnose NO_x emissions since vertical mixing can be a source of error in a surface-only comparison. With finer spatial resolution and more numerous NO_2 measurements now available from TEMPO starting in August 2023, it is feasible that a similar analysis could be conducted using satellite data. This project provides actionable information to policymakers looking to understand where there are further opportunities to reduce NO_x emissions and improve ozone and $PM_{2.5}$ air quality in metropolitan areas.

Acknowledgements. The authors of this paper would like to acknowledge the NASA Tropospheric Composition Program and the Texas Commission on Environmental Quality for TRACER-AQ support, and the TRACER-AQ science team for their useful contributions. The preparation of this manuscript was funded by a grant from the Texas Air Quality Research Program (AQRP) at The University of Texas at Austin through the Texas Emission Reduction Program (TERP) and the Texas Commission on Environmental Quality (TCEQ). The findings, opinions and conclusions are the work of the authors and do not necessarily represent findings, opinions, or conclusions of the AQRP or the TCEQ. The authors also acknowledge funding from the NASA Atmospheric Composition Modelling and Analysis Program (ACMAP) (80NSSC23K1002) and the NASA Health and Air Quality Applied Sciences Team (HAQAST) (80NSSC21K0511). This work contains modified Copernicus Sentinel-5 Precursor data processed by KNMI and post-processed by George Washington University.

Description of author's responsibilities. D.G., L.J., B.D. and G.Y. developed the project design. J.J. and G.Y. set-up and conducted the WRF-CAMx simulations. L.J. and the TRACER-AQ science team measured and processed the GCAS and Pandora Data. D.G downloaded and processed the TROPOMI NO_2 data and re-gridded all data to the WRF-CAMx grid. B.D. performed the flux divergence and ran the regression model. D.G., B.D., and M.O.N developed figures for the manuscript. D.G. and B.D. wrote the paper. All authors edited the manuscript.

Data availability. NO_2 observations from GCAS are available here: https://doi.org/10.5067/ASDC/SUBORBITAL/TRACERAQ/DATA001/GV/AircraftRemoteSensing/GCAS_1. The publicly available GCAS measurements (version R2) include a version of the dataset with reprocessed AMFs to include NO_2 vertical profile estimates from the fine-scale (444 × 444 m^2) WRF-CAMx simulation used in this analysis. TROPOMI NO_2 column data are publicly available from the Copernicus Data Space Ecosystem: https://dataspace.copernicus.eu. Pandora NO_2 data are available here: https://asdc.larc.nasa.gov/project/TRACER-AQ/TRACERAQ_Pandora_Data_1. WRF-CAMx output for NO_2 and O_3 are available upon request.

References

(1) Jin, X.; Fiore, A.; Boersma, K. F.; Smedt, I. De; Valin, L. Inferring Changes in Summertime Surface Ozone–NO x –VOC Chemistry over U.S. Urban Areas from Two Decades of Satellite and Ground-Based Observations. *Environ Sci Technol* **2020**, *54* (11), 6518–6529. https://doi.org/10.1021/acs.est.9b07785.

(2) Simon, H.; Reff, A.; Wells, B.; Xing, J.; Frank, N. Ozone Trends across the United States over a Period of Decreasing NOx and VOC Emissions. *Environ Sci Technol* **2015**, *49* (1), 186–195. https://doi.org/10.1021/es504514z.

(3) Simon, H.; Hogrefe, C.; Whitehill, A.; Foley, K. M.; Liljegren, J.; Possiel, N.; Wells, B.; Henderson, B. H.; Valin, L. C.; Tonnesen, G.; Appel, K. W.; Koplitz, S. Revisiting Day-of-Week Ozone Patterns in an Era of Evolving US Air Quality. *Atmos Chem Phys* **2024**, *24* (3), 1855–1871. https://doi.org/10.5194/acp-24-1855-2024.

(4) Koplitz, S.; Simon, H.; Henderson, B.; Liljegren, J.; Tonnesen, G.; Whitehill, A.; Wells, B. Changes in Ozone Chemical Sensitivity in the United States from 2007 to 2016. *ACS Environmental Au* **2021**, *2*, 206–222. https://doi.org/10.1021/ACSENVIRONAU.1C00029.

(5) Achakulwisut, P.; Brauer, M.; Hystad, P.; Anenberg, S. C. Global, National, and Urban Burdens of Paediatric Asthma Incidence Attributable to Ambient NO_2 Pollution: Estimates from Global Datasets. *Lancet Planet Health* **2019**. https://doi.org/10.1016/S2542-5196(19)30046-4.

(6) Anenberg, S. C.; Mohegh, A.; Goldberg, D. L.; Kerr, G. H.; Brauer, M.; Burkart, K.; Hystad, P.; Larkin, A.; Wozniak, S.; Lamsal, L. Long-Term Trends in Urban NO2 Concentrations and Associated Paediatric Asthma Incidence: Estimates from Global Datasets. *Lancet Planet Health* **2022**, *6* (1), e49–e58. https://doi.org/10.1016/S2542-5196(21)00255-2.

(7) Huang, K.; Zhu, Q.; Lu, X.; Gu, D.; Liu, Y. Satellite-Based Long-Term Spatiotemporal Trends in Ambient NO2 Concentrations and Attributable Health Burdens in China From 2005 to 2020. *Geohealth* **2023**, *7* (5), e2023GH000798. https://doi.org/10.1029/2023GH000798.

(8) Camilleri, S. F.; Kerr, G. H.; Anenberg, S. C.; Horton, D. E. All-Cause NO2-Attributable Mortality Burden and Associated Racial and Ethnic Disparities in the United States. *Environ Sci Technol Lett* **2023**. https://doi.org/10.1021/acs.estlett.3c00500.

(9) Zawacki, M.; Baker, K. R.; Phillips, S.; Davidson, K.; Wolfe, P. Mobile Source Contributions to Ambient Ozone and Particulate Matter in 2025. *Atmos Environ* **2018**, *188*, 129–141. https://doi.org/10.1016/j.atmosenv.2018.04.057.

(10) McDuffie, E. E.; Smith, S. J.; O'Rourke, P.; Tibrewal, K.; Venkataraman, C.; Marais, E. A.; Zheng, B.; Crippa, M.; Brauer, M.; Martin, R. V. A Global Anthropogenic Emission Inventory of Atmospheric Pollutants from Sector- and Fuel-Specific Sources (1970–2017): An Application of the Community Emissions Data System (CEDS). *Earth Syst Sci Data* **2020**, *12* (4), 3413–3442. https://doi.org/10.5194/essd-12-3413-2020.

(11) Crippa, M.; Guizzardi, D.; Muntean, M.; Schaaf, E.; Dentener, F.; van Aardenne, J. A.; Monni, S.; Doering, U.; Olivier, J. G. J.; Pagliari, V.; Janssens-Maenhout, G. Gridded Emissions of Air Pollutants for the Period 1970--2012 within EDGAR v4.3.2. *Earth Syst Sci Data* **2018**, *10* (4), 1987–2013. https://doi.org/10.5194/essd-10-1987-2018.

(12) Crippa, M.; Guizzardi, D.; Pisoni, E.; Solazzo, E.; Guion, A.; Muntean, M.; Florczyk, A.; Schiavina, M.; Melchiorri, M.; Hutfilter, A. F. Global Anthropogenic Emissions in Urban Areas: Patterns, Trends, and Challenges. *Environmental Research Letters* **2021**, *16* (7), 074033. https://doi.org/10.1088/1748-9326/AC00E2.
(13) Goldberg, D. L.; Lu, Z.; Streets, D. G.; de Foy, B.; Griffin, D.; McLinden, C. A.; Lamsal, L. N.; Krotkov, N. A.; Eskes, H. J. Enhanced Capabilities of TROPOMI NO2: Estimating NOx from North American Cities and Power Plants. *Environ Sci Technol* **2019**, *53* (21), 12594–12601. https://doi.org/10.1021/acs.est.9b04488.
(14) Beirle, S.; Boersma, K. F.; Platt, U.; Lawrence, M. G.; Wagner, T. Megacity Emissions and Lifetimes of Nitrogen Oxides Probed from Space. *Science (1979)* **2011**, *333* (6050), 1737–1739. https://doi.org/10.1126/science.1207824.
(15) Beirle, S.; Borger, C.; Dörner, S.; Li, A.; Hu, Z.; Liu, F.; Wang, Y.; Wagner, T. Pinpointing Nitrogen Oxide Emissions from Space. *Sci Adv* **2019**, *5* (11), eaax9800. https://doi.org/10.1126/sciadv.aax9800.
(16) Kuhlmann, G.; Chan, K. L.; Donner, S.; Zhu, Y.; Schwaerzel, M.; Dörner, S.; Chen, J.; Hueni, A.; Nguyen, D. H.; Damm, A.; Schütt, A.; Dietrich, F.; Brunner, D.; Liu, C.; Buchmann, B.; Wagner, T.; Wenig, M. Mapping the Spatial Distribution of NO2 with in Situ and Remote Sensing Instruments during the Munich NO2 Imaging Campaign. *Atmos Meas Tech* **2022**, *15* (6), 1609–1629. https://doi.org/10.5194/AMT-15-1609-2022.
(17) Meier, A. C.; Schönhardt, A.; Bösch, T.; Richter, A.; Seyler, A.; Ruhtz, T.; Constantin, D.-E.; Shaiganfar, R.; Wagner, T.; Merlaud, A.; Van Roozendael, M.; Belegante, L.; Nicolae, D.; Georgescu, L.; Burrows, J. P. High-Resolution Airborne Imaging DOAS Measurements of NO2 above Bucharest during AROMAT. *Atmos Meas Tech* **2017**, *10* (5), 1831–1857. https://doi.org/10.5194/amt-10-1831-2017.
(18) Souri, A. H.; Choi, Y.; Pan, S.; Curci, G.; Nowlan, C. R.; Janz, S. J.; Kowalewski, M. G.; Liu, J.; Herman, J. R.; Weinheimer, A. J. First Top-Down Estimates of Anthropogenic NOx Emissions Using High-Resolution Airborne Remote Sensing Observations. *Journal of Geophysical Research: Atmospheres* **2018**, *123* (6), 3269–3284. https://doi.org/10.1002/2017JD028009.
(19) Goldberg, D. L.; Lu, Z.; Oda, T.; Lamsal, L. N.; Liu, F.; Griffin, D.; McLinden, C. A.; Krotkov, N. A.; Duncan, B. N.; Streets, D. G. Exploiting OMI NO2 Satellite Observations to Infer Fossil-Fuel CO2 Emissions from U.S. Megacities. *Science of The Total Environment* **2019**, *695*, 133805. https://doi.org/10.1016/j.scitotenv.2019.133805.
(20) Lu, Z.; Streets, D. G.; de Foy, B.; Lamsal, L. N.; Duncan, B. N.; Xing, J. Emissions of Nitrogen Oxides from US Urban Areas: Estimation from Ozone Monitoring Instrument Retrievals for 2005-2014. *Atmos Chem Phys* **2015**, *15* (18), 10367–10383. https://doi.org/10.5194/acp-15-10367-2015.
(21) Liu, F.; Beirle, S.; Joiner, J.; Choi, S.; Tao, Z.; Knowland, K. E.; Smith, S. J.; Tong, D. Q.; Ma, S.; Fasnacht, Z. T.; Wagner, T. High-Resolution Mapping of Nitrogen Oxide Emissions in Large US Cities from TROPOMI Retrievals of Tropospheric Nitrogen Dioxide Columns. *Atmos Chem Phys* **2024**, *24* (6), 3717–3728. https://doi.org/10.5194/acp-24-3717-2024.
(22) Goldberg, D. L.; Anenberg, S. C.; Lu, Z.; Streets, D. G.; Lamsal, L. N.; E McDuffie, E.; Smith, S. J. Urban NOx Emissions around the World Declined Faster than Anticipated between 2005 and 2019. *Environmental Research Letters* **2021**, *16* (11), 115004. https://doi.org/10.1088/1748-9326/ac2c34.

(23) Goldberg, D. L.; Saide, P. E.; Lamsal, L. N.; de Foy, B.; Lu, Z.; Woo, J.-H.; Kim, Y.; Kim, J.; Gao, M.; Carmichael, G. R.; Streets, D. G. A Top-down Assessment Using OMI NO2 Suggests an Underestimate in the NOx Emissions Inventory in Seoul, South Korea, during KORUS-AQ. *Atmos Chem Phys* **2019**, *19* (3), 1801–1818. https://doi.org/10.5194/acp-19-1801-2019.
(24) de Foy, B.; Lu, Z.; Streets, D. G.; Lamsal, L. N.; Duncan, B. N. Estimates of Power Plant NOx Emissions and Lifetimes from OMI NO2 Satellite Retrievals. *Atmos Environ* **2015**, *116* (2), 1–11. https://doi.org/10.1016/j.atmosenv.2015.05.056.
(25) Beirle, S.; Borger, C.; Jost, A.; Wagner, T. Improved Catalog of NOx Point Source Emissions (Version 2). *Earth Syst Sci Data* **2023**, *15* (7), 3051–3073. https://doi.org/10.5194/essd-15-3051-2023.
(26) Goldberg, D. L.; Harkey, M.; de Foy, B.; Judd, L.; Johnson, J.; Yarwood, G.; Holloway, T. Evaluating NOx Emissions and Their Effect on O3 Production in Texas Using TROPOMI NO2 and HCHO. *Atmos Chem Phys* **2022**, *22* (16), 10875–10900. https://doi.org/10.5194/acp-22-10875-2022.
(27) Janz, S.; Kowalewski, M. G.; Lamsal, L. N.; Nowlan, C.; Judd, L. M. Airborne Hyperspectral Trace Gas Sensors as Testbeds for Geostationary Air Quality Missions. In *Sensors, Systems, and Next-Generation Satellites XXIII*; Neeck, S. P., Kimura, T., Martimort, P., Eds.; SPIE, 2019; Vol. 11151, p 86. https://doi.org/10.1117/12.2533765.
(28) Nowlan, C. R.; Liu, X.; Janz, S. J.; Kowalewski, M. G.; Chance, K. V.; Follette-Cook, M. B.; Fried, A.; González Abad, G.; Herman, J. R.; Judd, L. M.; Kwon, H.-A. A.; Loughner, C. P.; Pickering, K. E.; Richter, D.; Spinei, E.; Walega, J.; Weibring, P.; Weinheimer, A. J. Nitrogen Dioxide and Formaldehyde Measurements from the GEOstationary Coastal and Air Pollution Events (GEO-CAPE) Airborne Simulator over Houston, Texas. *Atmos Meas Tech* **2018**, *11* (11), 5941–5964. https://doi.org/10.5194/amt-11-5941-2018.
(29) *TRACER-AQ – TRacking Aerosol Convection ExpeRiment – Air Quality*. https://www-air.larc.nasa.gov/missions/tracer-aq/ (accessed 2022-08-09).
(30) Omar Nawaz, M.; Johnson, J.; Yarwood, G.; de Foy, B.; Judd, L.; Goldberg, L. An Intercomparison of Satellite, Airborne, and Ground-Level Observations with WRF-CAMx Simulations of NO2 Columns over Houston, TX during the September 2021 TRACER-AQ Campaign. *Atmos Chem Phys* **2024**. https://doi.org/10.5194/egusphere-2023-2844.
(31) Platt, U.; Stutz, J. Differential Optical Absorption Spectroscopy. *Differential Optical Absorption Spectroscopy* **2008**. https://doi.org/10.1007/978-3-540-75776-4.
(32) Judd, L. M.; Al-Saadi, J. A.; Janz, S. J.; Kowalewski, M. G.; Pierce, R. B.; Szykman, J. J.; Valin, L. C.; Swap, R.; Cede, A.; Mueller, M.; Tiefengraber, M.; Abuhassan, N.; Williams, D. Evaluating the Impact of Spatial Resolution on Tropospheric NO2 Column Comparisons within Urban Areas Using High-Resolution Airborne Data. *Atmos. Meas. Tech* **2019**, *12*, 6091–6111. https://doi.org/10.5194/amt-12-6091-2019.
(33) Judd, L. M.; Al-Saadi, J. A.; Szykman, J. J.; Valin, L. C.; Janz, S. J.; Kowalewski, M. G.; Eskes, H. J.; Veefkind, J. P.; Cede, A.; Mueller, M.; Gebetsberger, M.; Swap, R.; Pierce, R. B.; Nowlan, C. R.; Abad, G. G.; Nehrir, A.; Williams, D. Evaluating Sentinel-5P TROPOMI Tropospheric NO2 Column Densities with Airborne and Pandora Spectrometers near New York City and Long Island Sound. *Atmos Meas Tech* **2020**, *13* (11), 6113–6140. https://doi.org/10.5194/amt-13-6113-2020.
(34) Keller, C. A.; Knowland, K. E.; Duncan, B. N.; Liu, J.; Anderson, D. C.; Das, S.; Lucchesi, R. A.; Lundgren, E. W.; Nicely, J. M.; Nielsen, E.; Ott, L. E.; Saunders, E.;

Strode, S. A.; Wales, P. A.; Jacob, D. J.; Pawson, S. Description of the NASA GEOS Composition Forecast Modeling System GEOS-CF v1.0. *J Adv Model Earth Syst* **2021**, e2020MS002413. https://doi.org/10.1029/2020MS002413.

(35) Skamarock, W. C.; Klemp, J. B.; Dudhia, J.; Gill, D. O.; Liu, Z.; Berner, J.; Wang, W.; Powers, J. G.; Duda, M. G.; Barker, D. M.; Huang, X.-Y. *A Description of the Advanced Research WRF Model Version 4*; 2021. http://library.ucar.edu/research/publish-technote.

(36) Ramboll. *CAMx User's Guide Version 6.50*. http://www.camx.com/files/camxusersguide_v6-50.pdf.

(37) de Foy, B.; Schauer, J. J. An Improved Understanding of NOx Emissions in South Asian Megacities Using TROPOMI NO2 Retrievals. *Environmental Research Letters* **2022**, *17* (2), 024006. https://doi.org/10.1088/1748-9326/ac48b4.

(38) Lonsdale, C. R.; Sun, K. Nitrogen Oxides Emissions from Selected Cities in North America, Europe, and East Asia Observed by the TROPOspheric Monitoring Instrument (TROPOMI) before and after the COVID-19 Pandemic. *Atmos Chem Phys* **2023**, *23* (15), 8727–8748. https://doi.org/10.5194/acp-23-8727-2023.

(39) Sun, K. Derivation of Emissions from Satellite-Observed Column Amounts and Its Application to TROPOMI NO2 and CO Observations. *Geophys Res Lett* **2022**, e2022GL101102. https://doi.org/10.1029/2022GL101102.

(40) Hersbach, H.; Bell, B.; Berrisford, P.; Hirahara, S.; Horányi, A.; Muñoz-Sabater, J.; Nicolas, J.; Peubey, C.; Radu, R.; Schepers, D.; Simmons, A.; Soci, C.; Abdalla, S.; Abellan, X.; Balsamo, G.; Bechtold, P.; Biavati, G.; Bidlot, J.; Bonavita, M.; Chiara, G.; Dahlgren, P.; Dee, D.; Diamantakis, M.; Dragani, R.; Flemming, J.; Forbes, R.; Fuentes, M.; Geer, A.; Haimberger, L.; Healy, S.; Hogan, R. J.; Hólm, E.; Janisková, M.; Keeley, S.; Laloyaux, P.; Lopez, P.; Lupu, C.; Radnoti, G.; Rosnay, P.; Rozum, I.; Vamborg, F.; Villaume, S.; Thépaut, J. The ERA5 Global Reanalysis. *Quarterly Journal of the Royal Meteorological Society* **2020**, *146* (730), 1999–2049. https://doi.org/10.1002/qj.3803.

(41) de Foy, B.; Cui, Y. Y.; Schauer, J. J.; Janssen, M.; Turne, J. R.; Wiedinmyer, C. Estimating Sources of Elemental and Organic Carbon and Their Temporal Emission Patterns Using a Least Squares Inverse Model and Hourly Measurements from the St. Louis-Midwest Supersite. *Atmos Chem Phys* **2015**, *15* (5), 2405–2427. https://doi.org/10.5194/acp-15-2405-2015.

(42) Wagner, T.; Warnach, S.; Beirle, S.; Bobrowski, N.; Jost, A.; Pukite, J.; Theys, N. Investigation of Three-Dimensional Radiative Transfer Effects for UV-Vis Satellite and Ground-Based Observations of Volcanic Plumes. *Atmos Meas Tech* **2023**, *16* (6), 1609–1662. https://doi.org/10.5194/amt-16-1609-2023.

(43) Douros, J.; Eskes, H. J.; van Geffen, J. H. G. M. *Comparing Sentinel-5P TROPOMI NO2 column observations with the CAMS-regional air quality ensemble*. EGUsphere. https://egusphere.copernicus.org/preprints/2022/egusphere-2022-365/ (accessed 2022-07-04).

(44) Lambert, J.-C.; Claas, J.; Stein-Zweers, D.; Ludewig, A.; Loyola, D.; Sneep, M.; Dehn, A. *Quarterly Validation Report of the Copernicus Sentinel-5 Precursor Operational Data Products #19*; 2023.